REFERENCES

[1] L. K. Anderson, "An analysis of broadband circulators with external tuning elements," *IEEE Trans. Microwave Theory Tech.*, vol. MTT-15, pp. 42–47, Jan. 1967.

[2] V. Gelnovatch, "Design of distributed transistor amplifiers at microwave frequencies," *Microwave J.*, vol. 10, pp. 41–47, Jan. 1967.

[3] T. M. Reeder and D. K. Winslow, "Characteristics of microwave acoustic transducers for volume wave excitation," *IEEE Trans. Microwave Theory Tech.*, vol. MTT-17, pp. 927–941, Nov. 1969.

[4] H. W. Bode, *Network Analysis and Feedback Amplifier Design*. New York: Van Nostrand, 1945, pp. 360–371.

[5] R. M. Fano, "Theoretical limitations on the broadband matching of arbitrary impedances," *J. Franklin Inst.*, vol. 249, pp. 57–84 and 139–154, Jan.–Feb. 1950.

[6] G. L. Matthei et al., *Microwave Filters, Impedance Matching Networks, and Coupling Structures*. New York: McGraw-Hill, 1964.

[7] D. C. Youla, "A new theory of broad-band matching," *IEEE Trans. Circuit Theory*, vol. CT-11, pp. 30–50, Mar. 1964.

[8] E. Schwartz, "Broadband matching of resonant circuits and circulators," *IEEE Trans. Microwave Theory Tech.*, vol. MTT-16, pp. 158–165, Mar. 1968.

[9] T. N. Trick and J. Vlach, "Computer-aided design of broad-band amplifiers with complex loads," *IEEE Trans. Micrwovae Theory Tech.*, vol. MTT-18, pp. 541–547, Sept. 1970.

[10] P. H. Smith, *Electronic Applications of the Smith Chart*. New York: McGraw-Hill, 1969.

[11] H. C. Okean and H. Weingart, "S-band integrated parametric amplifier having both flat-gain and linear phase response," *IEEE Trans. Microwave Theory Tech.* (Corresp.), vol. MTT-16, pp. 1057–1059, Dec. 1968.

[12] J. E. Storer, *Passive Network Synthesis*. New York: McGraw-Hill, 1957, ch. 12.

[13] C. L. Ruthroff, "Some broad-band transformers," *Proc. IEEE*, vol. 47, pp. 1337–1342, Aug. 1959.

[14] C. P. Womack, "The use of exponential transmission lines in microwave components," *IEEE Trans. Microwave Theory Tech.*, vol. MTT-10, pp. 124–132, Mar. 1962.

# Analysis and Design of Dispersive Interdigital Surface-Wave Transducers

W. RICHARD SMITH, HENRY M. GERARD, AND WILLIAM R. JONES, SENIOR MEMBER, IEEE

*Abstract*—A comprehensive circuit model characterization of dispersive interdigital transducers with nonuniform electrode spacing is presented. The model is an extension of a three-port circuit which has been useful for representing periodic transducers. The extended model includes the effects of strong piezoelectric coupling whereby the acoustic waves and electric circuits interact, and it also accounts for reflections of acoustic waves which result from perturbations of the crystal surface by the metal electrodes. The inclusion of the latter effect is shown to be essential for explaining observed levels of triple-transit echos in filters and delay lines. The circuit model is used to derive a transducer design procedure which determines the electrode positions and the apodization function (acoustic aperture taper) required to reproduce a desired waveform. This procedure is applicable to the design of weighted dispersive filters and broad-band nondispersive delay lines. In order to verify the theory a low-loss octave-bandwidth nondispersive delay line was designed using linear FM dispersive transducers on $YZ$ LiNbO$_3$. The performance of this device was found to be in good agreement with the circuit model predictions.

## I. INTRODUCTION

ACOUSTIC WAVES propagating on the surface of a piezoelectric crystal provide a convenient means of implementing delay lines and filters at frequencies ranging from several megahertz to several hundred megahertz. In addition to the considerations of low propagation loss and microminiature dimensions which are basic to most acoustic devices, the surface-
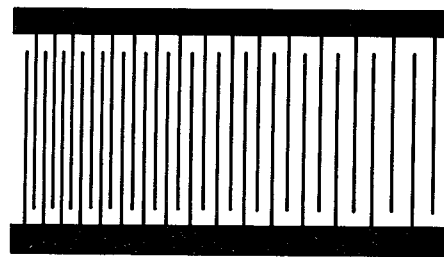
Fig. 1.   Electrode configuration in a dispersive interdigital transducer.

wave mode has the important advantage of providing continuous access to the propagating acoustic wave. This aspect of surface-wave delay lines has received considerable attention recently, particularly in connection with the synthesis of dispersive filters [1]–[6].

In order to realize the full potential of surface waves in filter and delay-line applications, it is necessary that the design of these devices be based on a model that accounts for all significant interactions among the electroacoustic transducer, the external electric circuit, and the acoustic waves propagating on the piezoelectric substrate. This paper extends a widely used circuit model for periodic (nondispersive) transducers to characterize (dispersive) transducers with nonuniformly spaced electrodes (see Fig. 1). The primary objectives of this work are to present the circuit model results in closed form wherever possible as a guide to dispersive transducer design, and to justify the use of this model by experimental verification.

The circuit model includes the electroacoustic interactions between the acoustic and electrical loading circuits. The analysis shows explicitly how these interactions determine the transducer response. It is demonstrated further that under certain conditions the results of this general circuit model reduce to those predicted by weak coupling theories which ignore electroacoustic interactions.

Emphasis is placed upon the linear FM transducer as applied to the design of broad-band nondispersive delay lines and highly dispersive filters. It is often desirable in these devices to implement spectral weighting by means of apodization, i.e., acoustic aperture weighting. Apodization is introduced in the circuit model and an expression is derived which determines the apodization law that is necessary to achieve a specified weighting. This result is applied to the design of a low-loss nondispersive delay line having a rectangular transfer function covering an octave bandwidth. The performance of this device, which is substantially as predicted, represents a significant advance in the state of the art of broad-band acoustic delay lines as well as a nontrivial validation of the circuit model design equations.

The circuit model is generalized to include an acoustic wave impedance difference between the electroded and nonelectroded regions. The primary manifestations of this electrode "loading" on the dispersive transducer are to introduce acoustic directivity and to increase the magnitude of the acoustic reflection coefficients. A value for the "loading" parameter is postulated on the basis of the electrode shorting effect which gives excellent agreement with measurement for aluminum on $YZ$ lithium niobate. The analysis is applied to the particularly interesting case of a highly dispersive filter with a time-bandwidth product of 1000. The computed results indicate that electrode "loading" can lead to strong acoustic reflections in devices with a large number of electrodes, particularly when high-coupling piezoelectric substrates are used.

This investigation augments recent theoretical and experimental studies of dispersive interdigital transducers [1]. Tancrell and Holland discuss dispersive transducer theory based on a weak-coupling "delta-function" model and provide evidence that some phenomena of transducer performance are not accounted for by such a model. They also show that most of the electroacoustic interaction phenomena can be predicted with a more detailed circuit model similar to the one presented in this paper. The authors, however, do not actually employ the detailed circuit model to refine transducer design.

## II. Equivalent Circuit Model

In order to obtain an equivalent circuit model for dispersive arrays we extend the "crossed-field" model for periodic transducers [7]. As discussed in [7], the surface-wave transducer configuration of Fig. 2(a) is approximated by the "crossed-field model" shown in
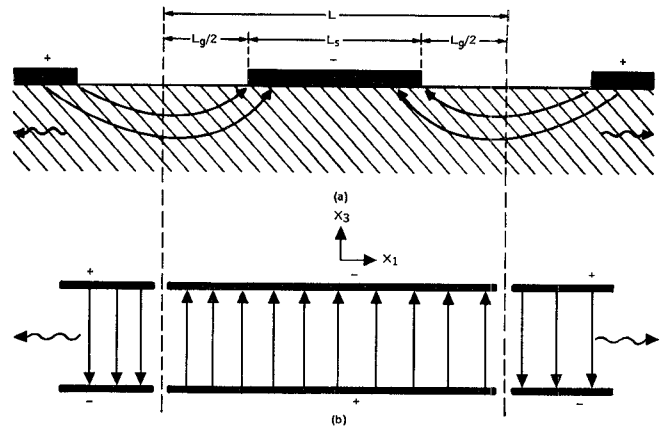


Fig. 2.   Crossed-field model approximation for surface waves. (a) Side view of unit cell of interdigital transducer, showing electrode and gap dimensions. (b) Crossed-field model for unit cell (one electrode).
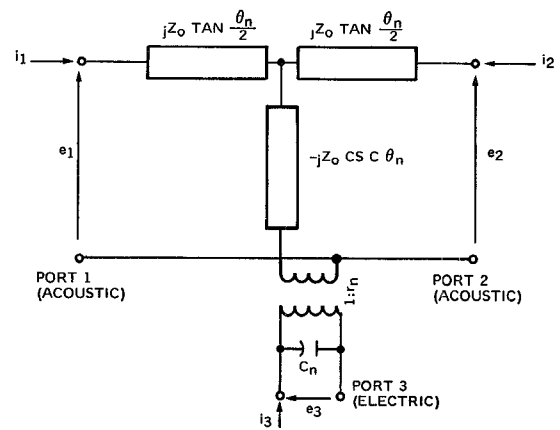


Fig. 3.   Mason equivalent circuit for the crossed-field model of a single-electrode section.

Fig. 2(b). It should be noted that [7] also contains an alternate ("in-line") circuit model which may be applicable for some substrate materials.[1] However, the "crossed-field" model was found to be best for characterizing transducers on $YZ$ lithium niobate and is mathematically simpler to use.

Since a dispersive transducer is not periodic, the basic "unit cell" or "section" consists of the region of length $L$ in Fig. 2(a), which corresponds to half the unit cell used in [7]. Furthermore, it is assumed that the static capacitance of the entire transducer is given by the sum of the nearest neighbor capacitances. This assumption has been verified experimentally [7] for periodic transducers and its validity in the dispersive case should require only that the dimensions $L$, $L_g$, $L_s$ vary slowly from section to section.

Each section of the dispersive transducer is represented by the Mason equivalent circuit shown in Fig. 3. In contrast with the periodic transducer model, different values of the circuit elements must be used for different

---

[1] This model is used for the circuit model analysis described in [1].

electrodes in the transducer. The terminal variables $e_1$, $e_2$ represent acoustic forces while $i_1$ and $i_2$ are the corresponding particle velocities. The static electrode capacitance of the $n$th section[2] is given by [8]

$$C_n = \frac{w_n \sqrt{\epsilon_{11}\epsilon_{33}}}{2} \frac{K(q_n)}{K(q_n')} \tag{1}$$

where $w_n$ is the acoustic aperture, $\epsilon_{11}$ and $\epsilon_{33}$ are the dielectric tensor components of the substrate, and $K$ is the Jacobian complete elliptic integral of the first kind with $q_n = \sin(\pi L_{sn}/2L_n)$ and $q_n' = (1-q_n^2)^{1/2}$. Note that $C_n$ is an increasing function of the electrode width-to-spacing ratio $L_{sn}/L_n$. Thus, in a dispersive comb which has constant electrode width, the high-frequency electrodes contribute more capacitance as they are more closely spaced.

The acoustic wave propagation in the $n$th section is represented by a transmission line whose characteristic impedance $Z_0$ corresponds to the mechanical impedance of the substrate which is taken to be the same in all sections.[3] $Z_0$ may be specified as unity without loss of generality since the electroacoustic transformer (described below) will always give the appropriate coupling to the electric circuit. The acoustic transit angle of the $n$th section is

$$\theta_n = \pi f / f_n \tag{2}$$

where $f_n$ is the synchronous frequency defined in terms of velocity and $L_n$ as

$$f_n = v/2L_n. \tag{3}$$

The acoustic aperture $w_n$ may in general be a function of $n$, and as such defines an *apodized* transducer. Indeed, the potential for designing dispersive filters with spectral weighting that is controlled by a prescribed $w_n$ function is a major advantage of acoustic surface-wave devices. A simple configuration which has been frequently used for constructing apodized combs is shown in Fig. 4(a). As demonstrated in [6], this geometry can lead to surface waves which are not straight-crested, resulting in significant degradation of transducer performance. As shown there, however, this problem can be corrected by designing the comb with added passive electrodes as shown in Fig. 4(b). In this paper we assume that apodized combs are constructed as in Fig. 4(b), so that it is unnecessary to account for nonplane wavefronts in the analysis.

The basic aim of this paper is to accommodate unequal apertures into the circuit model in such a way that a design prescription is obtained for apodized transducers. Spectral weighting by means of apodization is possible primarily because the apertures $w_n$ control the electroacoustic coupling via the transformer ratios $r_n$
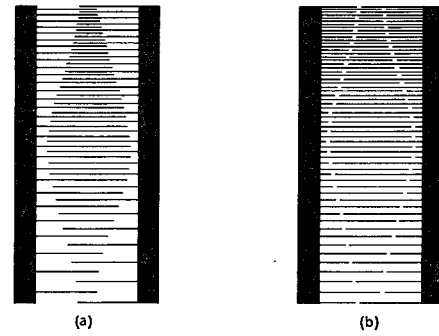


Fig. 4. Electrode configuration of apodized dispersive transducers. (a) Uncorrected comb. (b) Comb corrected with "dummy" electrodes to produce straight-crested surface waves.

shown in Fig. 3. The transformer ratio is given by

$$r_n = (-1)^n \sqrt{2f_n C_n k^2 Z_0} \cdot \left[ \frac{K(2^{-1/2})}{K(q_n)} \right] \tag{4}$$

where $k^2$ is the surface-wave electromechanical coupling constant. The elliptic integrals given in this equation and in (1) ensure that the effective electroacoustic coupling maximizes for $L_g = L_s$ and varies with stripe-to-gap ratio as described in [8]. Note, however, that the acoustic wave impedance $Z_0$ has the same value in the Mason circuits of all electrodes. This is appropriate because apodization weights the electroacoustic coupling but does not introduce any steps in the acoustic wave impedance which would cause acoustic reflections.

The value of $r_n$ given by (4) is proportional to $w_n^{1/2}$ and is used throughout the remainder of this paper. As such, it is applicable to delay lines and filters constructed with two identically apodized transducers in which most of the transduction at an operating frequency $f \cong f_n$ is accomplished by those electrodes of aperture $w \cong w_n$. This condition is satisfied by the experimental transducers described in this paper since the apertures $w_n$ do not vary appreciably over the region where the electrodes are synchronous with the acoustic wave to within approximately one half wavelength. Under this condition, the analysis of this paper yields virtually the same results as the multiple acoustic channel model described in [1]. When the apertures vary appreciably among the synchronous electrodes, the results may differ significantly so that the multichannel model is most appropriate for *analysis* even though it does not give a design prescription. Since both [1][4] and the present model ignore diffraction, the ultimate test of either model is experimental verification.

By implementing filters with one *apodized* transducer and one *unapodized* transducer, the present model can be extended to cases requiring that the transducer aper-

---

[2] Henceforth the subscript $n$ refers to quantities of the $n$th section.

[3] In Section IV we consider different values of $Z_0$ for the metallized and unmetallized regions and discuss the significance and consequences of this modification.

[4] Reference [1] finds an asymmetry in power flow with respect to the two acoustic ports (directions). This is a consequence of using the "in-line" Mason circuit model, and not because of using multiple acoustic channels in the analysis. This is an important difference between the "crossed-field" and "in-line" models when used for large combs and the appropriate model depends on the substrate material. See [7] and [10] for further details.
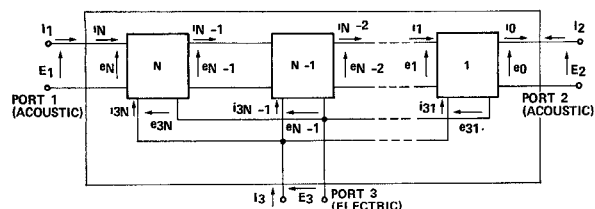
Fig. 5. Cascading configuration of single-electrode circuits to obtain a network for the $N$-electrode transducer.

tures vary appreciably over the region of synchronous electrodes. To accomplish this it is necessary to modify the analysis of this paper to account for the fact that part of the acoustic beam will "miss" the narrower electrodes of the apodized transducer. This can be accomplished by substituting $r_n' \cdot (w_n/w_{\max})^{1/2}$ for $r_n'$ in (17) and the ensuing results below. Filters of this type will be described in a subsequent paper.

A schematic three-port representation of a multielectrode interdigital transducer is shown in Fig. 5. This block diagram illustrates the manner in which the $N$ Mason circuits for individual electrodes must be interconnected to give an equivalent circuit for the entire transducer. This circuit includes the electric and acoustic interactions among all the electrodes in the transducer and is the circuit to be used in the three-port analysis for calculating transfer properties. $E_3$ and $I_3$ are electric terminal variables, while $E_1$, $E_2$ again represent acoustic forces and $I_1$, $I_2$ are particle velocities at the ends of the array.

The transducer may be characterized by the network admittance coefficients $Y_{ij}$, defined by

$$I_i = \sum_{j=1}^{3} Y_{ij} E_j \qquad (i = 1, 2, 3). \qquad (5)$$

It is assumed that the transducer is internally lossless,[5] so that the $Y_{ij}$ are purely imaginary. Using the admittance coefficients, the scattering and transmission characteristics of a transducer can be completely determined upon specification of the electric and acoustic terminal conditions. Fig. 6(a) and (b) illustrates transducer circuits corresponding to launching and reception, respectively, of acoustic waves. In the launch case the emergent acoustic waves are assumed to be absorbed without reflection from the ends of the substrate. This condition is represented by a "matched" termination $Z_0$ on each acoustic port. In the receive case the acoustic ports are again assumed to be matched and the electric port termination is purely resistive.

It is convenient to define a set of complex transfer functions $T_{ij}$ by

$$T_{ij} = 2 \sqrt{\frac{G_i}{G_j}} \frac{E_i}{E_j} \qquad (6)$$

where $E_i$ is the "voltage" of the transmitted or reflected

[5] Bulk wave excitation, ohmic losses, and propagation loss within the transducer are assumed to be negligible.
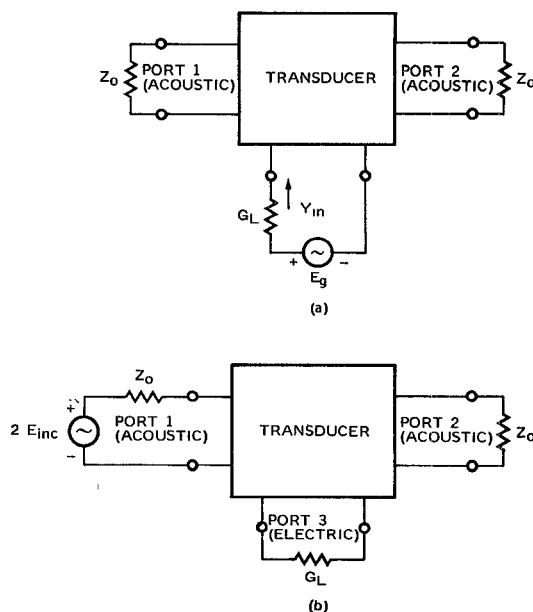


Fig. 6. Block diagram of launching and receiving transducer configurations. (a) Transducer with electric generator at port 3. (b) Transducer with acoustic generator at port 1.

wave delivered to a load $G_i$ at port $i$ when a Thévenin generator of voltage $E_j$ and series conductance $G_j$ drives the transducer at port $j$. These functions are normalized so that the power scattering coefficients are

$$p_{ij} = \frac{P_i}{(P_{\text{avail}})_j} = |T_{ij}|^2 \qquad (7)$$

where $P_i$ is the power transmitted or reflected from port $i$ and $(P_{\text{avail}})_j$ is the power available from a matched generator at port $j$. Thus $p_{ii}$ is the fraction of power reflected when power is incident at port $i$, and $p_{ij}$ $(i \neq j)$ is the fraction of power transmitted from port $i$ when power is incident at port $j$. By reciprocity $T_{ij} = T_{ji}$ and $p_{ij} = p_{ji}$. For convenience, power ratios are usually given in decibels and thus we define scattering loss in decibels by

$$L_{ij} = -10 \log_{10} (p_{ij}) \qquad \text{(dB)}. \qquad (8)$$

The two scattering quantities of greatest interest in delay lines and filters are the electroacoustic transfer functions $T_{13}$ and $T_{23}$ and acoustic reflection loss ($L_{11}$ or $L_{22}$). Throughout this paper, the expressions which appear for $T_{ij}$, $p_{ij}$, and $L_{ij}$ refer to the circuits of Fig. 6.

Since dispersive transducers are not periodic, it is not possible to write simple expressions for the admittance coefficients $Y_{ij}$ of the entire transducer. However, evaluation of the $Y_{ij}$ is straightforward with the aid of a digital computer program which makes use of the $y_{ij}$ coefficients of each electrode and the interconnection recursion relations given in Appendix A. In spite of the necessity of appealing to electronic computers to obtain explicit evaluation of the admittance coefficients, the "crossed-field" model can be effectively employed to explain, without computation, the salient features of dispersive transducer performance and design.

## III. Transducer Design

The problem of synthesizing electrical filters may be stated in terms of a desired transfer function

$$H(f) = E(f) \exp\left[j\Phi(f)\right].\qquad(9)$$

This form is often used for lumped-element filters designed from the viewpoint of weighting the spectral components of a signal. The same problem may be posed in an alternate fashion by specifying the desired impulse response

$$h(t) = e(t)\exp\left[j\phi(t)\right]\qquad(10)$$

which is the Fourier transform of $H(f)$. The latter form has found wide usage for distributed circuits involving time delay such as radar pulse compression and expansion filters.

Here we address the design problem by using the circuit model to determine the electrode positions $(t_n)$ and apodization $(w_n)$ which specify the best transducer design for generating the specified signal. In developing the design procedure we find it convenient to utilize both forms, $H(f)$ and $h(t)$, for the desired signal.[6] Because the circuit model analysis is developed in the frequency domain, the design problem is conveniently stated as

$$\left.\begin{array}{c}T_{13}(f)\\[2ex]\text{or}\qquad\qquad\\[2ex]T_{23}(f)\end{array}\right\} \cong \text{const } H(f)\qquad(11)$$

where $T_{13}$ and $T_{23}$ are the transfer functions defined in (6). However, the resultant design formulas will be expressed in terms of $h(t)$ because a transducer essentially takes *time samples* of a waveform. Each electrode corresponds to a well-defined temporal position on the substrate, but is capable of coupling electric and acoustic signals over a range of frequencies. Consequently, when a transducer transfer function $H(f)$ is specified, it is first necessary to calculate the associated time response $h(t)$ by a Fourier transformation.

We begin by deriving a convenient formula for $T_{13}(f)$. An important quantity which arises in the calculation of $T_{13}(f)$ is the electric input admittance $Y_{\text{in}}$ diagrammed in Fig. 6(a). When using the crossed-field model, it is convenient to separate $Y_{\text{in}}$ into the electrostatic capacitive susceptance in parallel with an acoustically generated radiation admittance, viz,

$$Y_{\text{in}} = Y_{\text{rad}} + j2\pi f C_T.\qquad(12)$$

An explicit formula for $Y_{\text{rad}}$ appears in Appendix B. With the choice of a convenient reference frequency $f_0$, a dimensionless radiation admittance can be defined by

$$y_{\text{rad}}(f) = Q_r Y_{\text{rad}}(f)/2\pi f_0 C_T\qquad(13)$$

⁶ Henceforth we assume that the desired signal, $H(f)$ or $h(t)$, refers to *one transducer*; the desired transfer functions for the two transducers in a filter must be chosen such that their product equals the desired *filter* transfer function. It is assumed that $p_{11} \ll 1$ and $p_{22} \ll 1$.

where

$$Q_r = 2\pi f_0 C_T / \text{Re}\left[Y_{\text{rad}}(f_0)\right]\qquad(14)$$

is called the "radiation $Q$." We also define a load $Q$ by

$$Q_L = 2\pi f_0 C_T / G_L\qquad(15)$$

and introduce a normalization for the transformer turn ratios (4), given by

$$r_n{}' = r_n\sqrt{\frac{Q_r}{\pi f_0 C_T}} = \sqrt{\frac{2k^2 Q_r}{\pi}\frac{f_n C_n}{f_0 C_T}}.\qquad(16)$$

It is shown in Appendix B that $|T_{23}| = |T_{13}|$ and that

$$T_{13}(f) = \sqrt{\frac{2Q_L}{Q_r}}\frac{\displaystyle\sum_{n=1}^{N} r_n{}' \sin\left(\frac{\pi}{2}\frac{f}{f_n}\right)\exp\left(-j2\pi f t_n\right)}{1 + jQ_L\left(\dfrac{f}{f_0}\right) + \dfrac{Q_L}{Q_r} y_{\text{rad}}(f)}\qquad(17)$$

where $t_n$ specifies the temporal position of the $n$th electrode. In this form, $T_{13}$ is normalized such that $|T_{13}|^2 = p_{13}$, while $y_{\text{rad}}$ and the sum in the numerator have magnitude near unity. The parameter $Q_r$ is inversely proportional to the coupling constant $(k^2)$ of the piezoelectric substrate and also depends on the transducer geometry. In general, the complexity of the function $Y_{\text{rad}}$ requires that $Q_r$ be calculated by evaluating $Y_{\text{rad}}$ on a computer. However, under certain conditions the transducer may be viewed approximately as a smaller periodic transducer centered at the synchronous electrodes [11], thus allowing hand-calculated estimates of $Q_r$. In most broad-band transducers, $Q_r \gg 1$ on even the strongest coupling piezoelectric substrates.

The load $Q(Q_L)$ is controlled by the impedance level of the external electric networks and by the acoustic apertures insofar as they determine the transducer capacitance $C_T$. Maximizing the transducer efficiency $(p_{13})$ calls for

$$Q_L{}^2 = \frac{Q_r{}^2}{1 + Q_r{}^2} \cong 1\qquad(18)$$

since we have assumed a resistive electric termination. Low values of $Q_L$ ($Q_L < 1$) tend to lower the transducer efficiency $(p_{13})$ and cause the transducer to pass, undisturbed, a large fraction of incident surface-wave power (i.e., large $p_{12}$; small $p_{11}$, $p_{22}$). This situation is desirable for applications which require weakly coupled tapping transducers with low multiple echo levels. When $Q_L \ll 1$, the circuit model results reduce to those which can be predicted by weak-coupling theories that ignore interactions between electrodes. Large values of $Q_L$ ($Q_L > 1$) cause the transducer to reflect acoustic energy (i.e., $p_{11}$ and $p_{22}$ approach unity) and should, therefore, generally be avoided. The choice of a value for $Q_L$ is the first step in transducer design. Since in practice the admittance $(G_L)$ of the electric loads is usually fixed, the chosen

value of $Q_L$ will dictate the required total capacitance $(C_T)$ determining thereby the scale factor for the apertures $(w_n)$.

The most important application of (17) is the determination of electrode positions $(t_n)$ and apertures $(w_n \propto (r_n')^2)$ for solving the waveform design problem posed in (11). In carrying out this design, we neglect in (17) the term $(Q_L/Q_r)y_{\text{rad}}(f)$ since, in most cases, $|(Q_L/Q_r)y_{\text{rad}}(f)| \ll |1+jQ_L(f/f_0)|$. We first rearrange (17) to define a new transfer function

$$\tilde{T}_{13}(f) = T_{13}(f)\left(1 + jQ_L\frac{f}{f_0}\right)$$

$$\cong \sqrt{\frac{2Q_L}{Q_r}}\sum_{n=1}^{N} r_n' \sin\left(\frac{\pi}{2}\frac{f}{f_n}\right)\exp\left(-j2\pi f t_n\right). \quad (19)$$

This leads to a restatement of the design problem

$$\tilde{T}_{13}(f) = \text{const}\, \tilde{H}(f) \quad (20)$$

where $\tilde{H}(f)$ is the Fourier transform of a new time signal $\tilde{h}(t)$, defined in terms of $h(t)$ by

$$\tilde{h}(t) = h(t) + \frac{Q_L}{2\pi f_0}\dot{h}(t)$$

$$= \left\{\left[e(t) + \frac{Q_L}{2\pi f_0}\dot{e}(t)\right]^2 + \left[\frac{Q_L}{2\pi f_0}e(t)\dot{\phi}(t)\right]^2\right\}^{1/2}$$

$$\cdot\exp\left\{j\phi(t) + j\tan^{-1}\left[\frac{Q_L e(t)\dot{\phi}(t)}{2\pi f_0 e(t) + Q_L \dot{e}(t)}\right]\right\} \quad (21)$$

where the dot notation is employed for differentiation with respect to time. The motivation for this restatement lies in the form of the right-hand side of (19). Appendix C shows, for a general time signal $b(t) = a(t)\exp[j\theta(t)]$, that

$$\int_{-\infty}^{\infty}dt\, a(t)\exp[j\theta(t)]\sum_{n=1}^{N}\{\delta[\theta(t) - (n + \tfrac{1}{2})\pi]$$

$$+ \delta[\theta(t) - (n - \tfrac{1}{2})\pi]\}\exp[-j2\pi f t]$$

$$\cong \sum_{n=1}^{N}\frac{a(t_n)(-1)^n}{\dot{\theta}(t)\big|_{t=t_n}}\sin\left(\frac{\pi}{2}\frac{f}{f_n}\right)\exp\left(-j2\pi f t_n\right) \quad (22)$$

when $a(t)$ and $\theta(t)$ are smooth functions of $t$ and

$$\theta(t_n) = n\pi, \qquad n = 1, 2, \cdots, N. \quad (23)$$

Therefore, the right-hand side of (22) gives the spectrum obtained by sampling a time signal $b(t)$ at times $t$ such that $\theta(t) = (n \pm 1/2)\pi$. Applying this result to sample $\tilde{h}(t)$ gives a spectrum which may be identified with the right-hand side of (19), thus determining $t_n$ and $r_n'$. This leads to the electrode positioning formula

$$\phi(t_n) + \tan^{-1}\left\{\frac{Q_L e(t_n)\dot{\phi}(t_n)}{2\pi f_0 e(t_n) + Q_L \dot{e}(t_n)}\right\} = n\pi,$$

$$n = 1, 2, \cdots, N. \quad (24)$$

The coefficients $r_n'$ are identified as

$$r_n' = \text{const}\frac{(-1)^n}{f_n}\left\{\left[e(t_n) + \frac{Q_L}{2\pi f_0}\dot{e}(t_n)\right]^2\right.$$

$$\left. + \left[\frac{Q_L}{2\pi f_0}e(t_n)\dot{\phi}(t_n)\right]^2\right\}^{1/2} \quad (25)$$

where we note that $f_n$ defined in (3), also corresponds to

$$f_n = \frac{1}{2\pi}\frac{d}{dt}\left\{\phi(t) + \tan^{-1}\left[\frac{Q_L e(t)\dot{\phi}(t)}{2\pi f_0 e(t) + Q_L \dot{e}(t)}\right]\right\}\bigg|_{t=t_n}. \quad (26)$$

By using (1), (4), and (16) we can specify the actual apertures $w_n$ rather than the coefficients $r_n'$, viz.,

$$w_n = A\left(\frac{f_n}{f_0}\right)^{-3}\frac{K(q_n)K(q_n')}{[K(2^{-1/2})]^2}\left\{\left[e(t_n) + \frac{Q_L}{2\pi f_0}\dot{e}(t_n)\right]^2\right.$$

$$\left. + \left[\frac{Q_L}{2\pi f_0}e(t_n)\dot{\phi}(t_n)\right]^2\right\} \quad (27)$$

where $K(q_n')$ and $K(q_n)$ are defined in conjunction with (1). The constant $A$ is most easily evaluated by requiring that the total capacitance $(C_T)$ satisfy (15), since $G_L$ and $Q_L$ are presumed to have been specified at the outset. Equations (24) and (27) indicate that both the electrode positions and apertures required to produce the waveform $h(t)$ will in principle depend on the external electric circuit via the load parameter $Q_L$.

It is of particular interest to specialize the design formulas to the problem of producing the linear FM waveform

$$h(t) = e(t)\exp\left[j2\pi\left(f_0 t + \frac{\Delta}{T}\frac{t^2}{2}\right)\right]$$

with

$$e(t) = \begin{cases}1, & |t| < T/2 \\ 0, & |t| > T/2.\end{cases} \quad (28)$$

The parameter $\Delta$ is the bandwidth and $f_0$ the center frequency of the chirped signal. Since $\dot{e}(t) = 0$ and $\dot{\phi}(t) = 2\pi(f_0 + (\Delta/T)t)$, the electrodes must have the temporal positions $t_n$ determined from (24) by

$$2\pi\left(f_0 t_n + \frac{\Delta}{T}\frac{t_n^2}{2}\right) + \tan^{-1}\left\{\frac{Q_L}{f_0}\left(f_0 + \frac{\Delta}{T}t_n\right)\right\}$$

$$= \left(n - \frac{N}{2}\right)\pi, \qquad n = 1, 2, \cdots, N. \quad (29)$$

The term $-N\pi/2$ on the right-hand side of (29) has been added because the signal specified by (28) is centered about $t = 0$. The apertures $(w_n)$ are given from (27) by

$$w_n = A\left(\frac{f_n}{f_0}\right)^{-3}\left[1 + \left(Q_L\frac{\dot{\phi}(t_n)}{2\pi f_0}\right)^2\right]\frac{K(q_n)K(q_n')}{K(2^{-1/2})^2} \quad (30)$$

where

$$\frac{f_n}{f_0} = 1 + \frac{\Delta}{f_0}\frac{t_n}{T} + \frac{1}{2\pi}\left[\frac{Q_L\frac{\Delta}{f_0}\frac{1}{f_0 T}}{1 + Q_L{}^2\left(1 + \frac{\Delta}{f_0}\frac{t_n}{T}\right)^2}\right]. \quad (31)$$

Inasmuch as

$$1 + \frac{\Delta}{f_0}\frac{t_n}{T} = \frac{\phi(t_n)}{2\pi f_0}$$

it is easily seen that

$$\frac{f_n}{f_0} \simeq \frac{\phi(t_n)}{2\pi f_0} \quad (32)$$

provided

$$Q_L\frac{\Delta}{f_0} \ll 1. \quad (33)$$

Subject to this condition, $w_n$ assumes the form

$$w_n = A\left(\frac{f_n}{f_0}\right)^{-3}\left[1 + Q_L{}^2\left(\frac{f_n}{f_0}\right)^2\right]\frac{K(q_n)K(q_n')}{K(2^{-1/2})^2} \quad (34)$$

and the relative positions of the electrodes, as determined by (24), differ negligibly from those specified by the classical linear FM prescription

$$2\pi f_0 t_n + \frac{\Delta}{T}\frac{t_n{}^2}{2} = n\pi + \text{const.} \quad (35)$$

The ratio of elliptic integrals $K(q_n)K(q_n')/K(2^{-1/2})^2$ may be replaced by unity if the electrodes are fabricated such that $L_{sn} = L_{gn}$. Thus when the condition (33) is satisfied, the parameter $Q_L$ has little effect on the electrode positions, but it is important in the aperture design.

In order to demonstrate the use of the design procedure developed here we consider the linear FM waveform (28) with $T = 1.05$ $\mu$s, $f_0 = 100$ MHz, and $\Delta = 46.7$ MHz. These parameters correspond to experimental transducers described in Section V. The Fourier transform of (28) is the desired function in the frequency domain, and is given by

$$H(f) = \sqrt{\frac{T}{2\Delta}}\left[Z(u_2) - Z(u_1)\right]$$

$$\cdot \exp\left[-j\pi\frac{T}{\Delta}(f - f_0)^2\right] \quad (36)$$

where $Z(u)$ is the complex Fresnel integral and

$$u_{1,2} = -2(f - f_0)\sqrt{\frac{T}{2\Delta}} \mp \sqrt{\frac{\Delta T}{2}}. \quad (37)$$

The foregoing analysis indicates that the optimum transducer for generating the signal specified by (28) or its equivalent, (36), should be designed according to
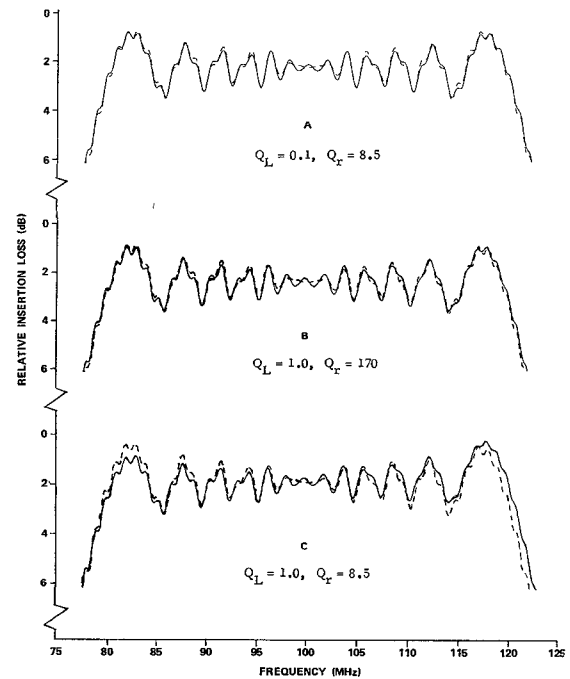


Fig. 7. Comparison of circuit model response $L_{13}$ of an apodized linear FM transducer to the exact linear FM spectrum. Dashed curves—linear FM spectrum $-10\log_{10}|H(f)|^2$. Solid curves—$L_{13}$ from circuit model.

(29) and (30) or, to an excellent approximation, according to (34) and (35). Consequently, we have carried out the design for three different combinations of $Q_L$ and $Q_r$, using (34) and (35). Fig. 7 compares the desired transfer function, $-10\log_{10}|H(f)|^2$ (dashed curve, three copies), to $L_{13}$ (solid curves). The solid and dashed curves are superimposed in each case by renormalizing $L_{13}$.

Case $A$ ($Q_L = 0.1$, $Q_r = 8.5$) assumes a $YZ$ lithium niobate substrate but, because $Q_L = 0.1$, the coupling is weak. In (17) the term $(Q_L/Q_r)y_{\text{rad}}(f)$ is negligible consistent with the design procedure. The apodization, from (34), is $w_n \propto f_n{}^{-3}$ to an excellent approximation. Curve $A$ shows that $L_{13}$ is very nearly identical to the desired transfer function. The small differences between the solid and dashed curves arise from comparing the spectrum of a continuous waveform to the sampling effected by a transducer.

Case $B$ ($Q_L = 1.0$, $Q_r = 170$) is designed to illustrate the accuracy of the approximations (34) and (35) for the value of $Q_L$ which minimizes insertion loss. In order to maintain the condition $|(Q_L/Q_r)y_{\text{rad}}(f)| \ll 1$, we assumed a $YX$ quartz substrate, giving $Q_r = 170$. Consequently, the agreement between $L_{13}$ and the desired transfer function is almost as good in curve $B$ as in the previous design (curve $A$). The main difference in $L_{13}$ is that the small amplitude ripples of frequency $\approx 1$ MHz are slightly skewed so as to be larger at the low-frequency end of the passband. This phenomenon is attributed to use of the approximations (34) and (35) in place of (29) and (30) when the condition (33) is only marginally satisfied.
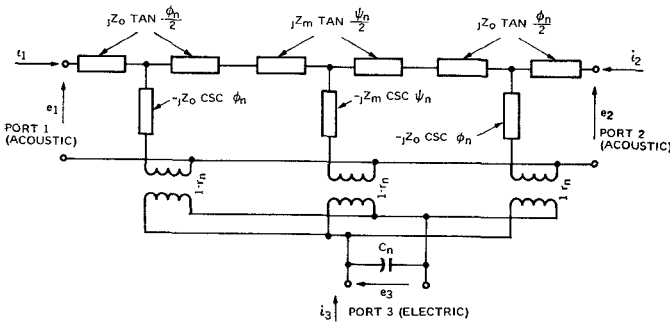
Case $C$ illustrates the additional error incurred when

Fig. 8. Mason equivalent circuit for the crossed-field model of one electrode, including an acoustic impedance discontinuity.

the term $(Q_L/Q_r)y_{rad}(f)$ is not negligible in (17). The parameters $Q_L = 1$, $Q_r = 8.5$ correspond to a $YZ$ lithium niobate substrate with the transducers loaded for minimum insertion loss. The result of neglecting $(Q_L/Q_r)y_{rad}$ in the design is that a ramp appears on $L_{13}$, giving higher transducer efficiency at the high-frequency end of the passband. Inasmuch as $L_{13}$ tapers by only 0.5 dB over the operating bandwidth, we consider the design procedure to be quite accurate for $Q_L/Q_r \leq 0.1$. For larger values of this ratio, the design procedure is still useful for obtaining preliminary designs which can be iteratively corrected to account for the term $(Q_L/Q_r)y_{rad}(f)$ in (17).

## IV. Acoustic Impedance Discontinuity Caused by Metal Electrodes

The preceding section describes the design of surface-wave transducers which give specified time waveforms. It shows that the design procedure may be applied to strong as well as weak-coupling piezoelectrics. In this section the basic transducer circuit model is extended to include the presence of the metal electrodes. When the effects described herein are significant, the preceding design formalism may also require modification. The extension described in this section is for purposes of analysis rather than design.

When a surface acoustic wave passes under an interdigital transducer, it encounters discontinuities in elastic and electrical properties as it traverses alternately metallized and unmetallized regions [12], [13]. For very thin electrodes, the primary source of discontinuity is the shorting of the tangential electric field by the metal, which lowers the acoustic velocity as discussed in [9] and [14]. Thicker electrodes also influence the elastic properties [15], [16] and introduce dispersion in the metallized regions. In order to estimate the effects of the discontinuities, the Mason circuit described in Section II is modified as shown in Fig. 8. The metallized region is represented by an acoustic transmission line of impedance $Z_m$, and transit angle $\psi_n = 2\pi f L_{sn}/v_m$, where $v_m$ is the acoustic velocity in the metallized region.[7] Each

---

[7] As a first-order approximation, the fact that $v_m$ is dispersive when the metallized region is of finite thickness has been neglected.

unelectroded portion has impedance $Z_0$ and transit angle $\phi_n = \pi f L_{gn}/v_0$, where $v_0$ is the surface-wave velocity of the unmetallized region. The total transit angle, $\psi_n + 2\phi_n$, corresponds to the single angle $\theta_n$ in the simple circuit of Fig. 3. No distinction is made in the turns ratios of the three transformers, all of which are given by (4). The defining equation for the synchronous frequency of the $n$th section becomes

$$f_n = \frac{1}{2} \left\{ \frac{L_{sn}}{v_m} + \frac{L_{gn}}{v_0} \right\}^{-1}. \tag{38}$$

The difference in acoustic velocities between metallized and unmetallized regions has little direct significance, because one can always adjust the values of $L_{gn}$, $L_{sn}$ to obtain any desired acoustic transit angles $\psi_n$, $\phi_n$. In doing so, the effect on the electrostatic capacitance contribution $C_n$ is small. The most important result is that the difference between $Z_m$ and $Z_0$ causes reflections of acoustic waves at the electrode-gap boundaries. Although these reflections are small for any single electrode, the reflections of many electrodes can add in phase to give a strong total reflection in a large array. This effect has received notable attention in the literature with regard to surface-wave gratings [17], passive delay lines [18], and phase-coded surface-wave delay lines [19].

To a large extent, surface-wave efforts have been concentrated at frequencies below a few hundred megahertz where the electrodes are sufficiently thin that the shorting of the tangential electric field is the principal cause of impedance discontinuity. In a rigorous analysis of surface waves in anisotropic media, it is not generally possible to define a scalar wave impedance in keeping with a transmission line characterization of wave propagation. Nevertheless, we have made an assumption which is a logical extension of the one-dimensional crossed-field model, namely that we can use a scalar acoustic impedance which is proportional to the surface-wave velocity.[8] Thus for the transducers considered in this paper we have taken

$$\tau = \frac{Z_0}{Z_m} = \frac{v_0}{v_m} \cong 1 + \frac{1}{2} k^2. \tag{39}$$

Note that the impedance discontinuity is proportional to the electromechanical coupling constant.

When the impedance discontinuity is included in the crossed-field Mason circuits of dispersive transducers, the principal results are as follows.

1) Introduction of acoustic directivity so that

$$p_{31} \neq p_{32} \text{ and } p_{11} \neq p_{22}.$$

2) Increase in magnitude of $p_{11}$ and $p_{22}$, thus increasing the level of multiple transit echoes in delay lines (or,

---

[8] This assumption is consistent with a definition that is basic to the original bulk wave derivation of the crossed-field Mason circuit, namely that acoustic wave impedance is equal to mass density times acoustic velocity.

equivalently, increasing the level of ripple on the delay line spectrum). The impedance discontinuity often gives the dominant contribution to $p_{11}$ and $p_{22}$.

*3) Introduction of additional ripple on the $p_{ij}$ transfer functions of a single transducer, usually to a lesser degree than the increase of multiple transit ripple previously mentioned.*

In short arrays the above effects are usually small. However, an example of a practical device where the impedance discontinuity is critically important is a highly dispersive filter with a compression ratio on the order of 1000 fabricated on a high-coupling piezoelectric material. Accordingly, we have computed the insertion loss function of such a filter configured with two identical linear FM transducers, each having 3601 electrodes. The two transducers are positioned as mirror images with the high-frequency ends closest together. The desired time signal is essentially that given by (28) with $f_0 = 300$ MHz, $\Delta = 120$ MHz, and $T = 6$ $\mu$s. However, we specify a modified envelope function

$$e(t) = \begin{cases} 1, & |t| < \dfrac{5T}{12} \\[2mm] \cos^2\left[\dfrac{6\pi}{T}\left(t - \dfrac{5T}{12}\right)\right], & \dfrac{5T}{12} < |t| < \dfrac{T}{2} \\[2mm] 0, & |t| > \dfrac{T}{2} \end{cases} \quad (40)$$

which tapers smoothly to zero at the ends of the time interval corresponding to the transducer length. This envelope taper helps suppress the Fresnel ripples which would appear on the transfer function $T_{13}$ of linear FM transducers designed for a rectangular envelope as in (28). The suppression of these ripples is often desirable in pulse compression applications.

For comparison, two substrate materials were considered: *YZ* (*Y*-cut, *Z*-propagating) lithium niobate (strong coupling) and *YX* quartz (weak coupling). In both cases the aperture and electric load were chosen to give $Q_L = 1$, thereby maximizing $p_{31}$.

The electrode positions were chosen according to (35) inasmuch as this design results in little error in the transfer function (cf., Fig. 7) even when (33) is only marginally satisfied. The apertures were specified according to (27) and it was noted that for this design the term $Q_L \dot{e}(t_n)/2\pi f_0$ is negligible. The ratio of elliptic integrals $K(q_n)K(q_n')/K(2^{-1/2})^2$ in (27) is unity, since the electrode and gap widths were chosen to give $L_{sn} = L_{gn}$.

Remembering that the design equations in Section III are based on the assumption $|(Q_L/Q_r)y_{\rm rad}(f)| \ll |1 + jQ_L(f/f_0)|$, we note that this condition is quite well satisfied for quartz ($Q_r \cong 120$). It is also rather well satisfied for lithium niobate but, with $Q_r \cong 6$, the term $(Q_L/Q_r)y_{\rm rad}(f)$ in (17) gives rise to a slight error. In order to achieve a flat spectrum, a small correction was made to the $w_n$ to account for the $y_{\rm rad}(f)$ term computed for the design described by (34). This resulted in an
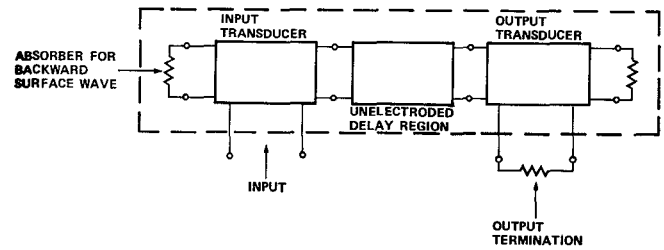


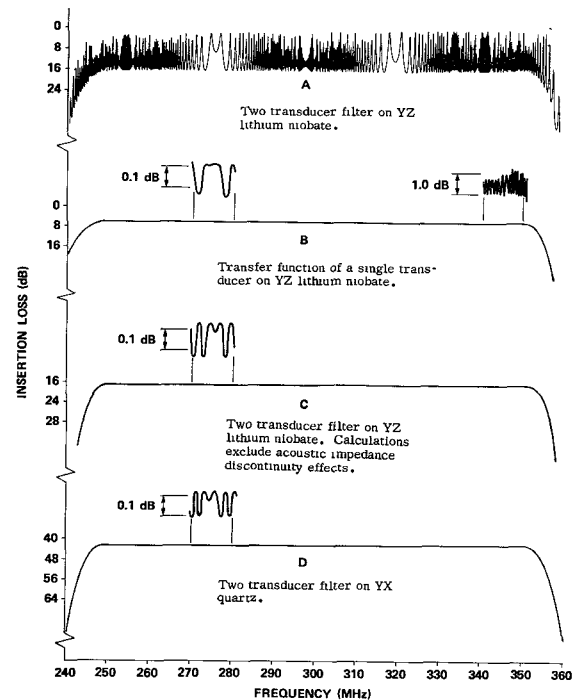Fig. 9. Block diagram of two transducers in a conventional delay line or filter configuration.



Fig. 10. Computed insertion loss for a 1000:1 linear FM dispersive filter demonstrating the effect of acoustic impedance discontinuities.

apodization law for the lithium niobate filter given by

$$w_n = w_0 e(t_n)(f_n/f_0)^{-3}[1.32 + (0.52 + 0.48 f_n/f_0)^2]. \quad (41)$$

Using a computer program based on the circuit model and the block diagram of Fig. 9, we have evaluated the insertion loss function of the two-transducer filter. In the computation, the unelectroded delay region between transducers has zero length although in an actual device some separation is needed to suppress electromagnetic feedthrough between the transducers. Acoustic propagation loss has been neglected in the calculation. The results, for both lithium niobate and quartz, are shown in Fig. 10.

Curve *A* shows the insertion loss function of the *YZ* lithium niobate filter. The impedance discontinuity parameter, from (39), is $\tau = 1.022$.[9] Although the insertion loss averages only 12 dB with a generally rectangular envelope, a very serious *triple-transit ripple* appears

---

[9] The assumed value of $k^2$, 0.044, is about 10 percent lower than that calculated in [9], and as such, is consistent with measurements of periodic transducers on *YZ* lithium niobate [7].
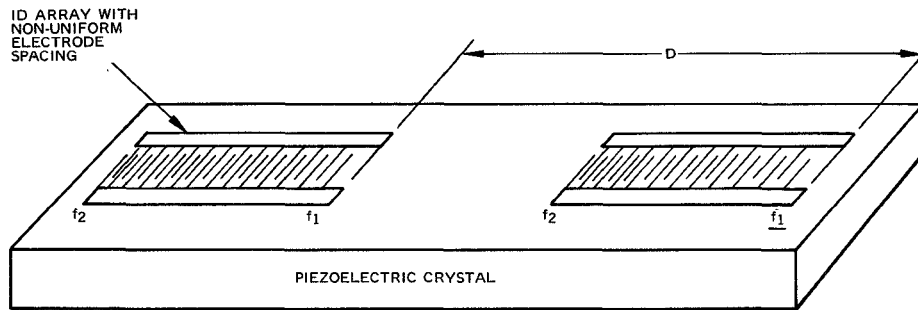
Fig. 11.   Nondispersive delay line configuration using identical dispersive transducers.

on the insertion loss function. It is clear that this ripple is due to the triple-transit phenomenon: First, the calculation yielded the additional information $2L_{11} = 5$ dB, and second, curve $B$ shows the relatively smooth insertion loss function $(L_{31})$ of a single transducer. It is equally clear that the triple-transit echoes are caused almost entirely by the acoustic impedance discontinuities of the electrodes. When the calculation was repeated with $\tau$ set equal to unity, thereby ignoring the impedance discontinuities, we obtained the filter insertion loss function shown in curve $C$. The remaining triple-transit ripples are discernible only on the expanded scale. The triple-transit suppression for $\tau = 1$ is $2L_{11} = 40$ dB.

Comparison of curves $A$ and $C$ shows a second phenomenon caused by the impedance discontinuities. The average insertion loss with the impedance discontinuities present (curve $A$) is some 6 dB lower. This is because the impedance discontinuities introduce directivity into the transducers, thus increasing the efficiency of coupling to acoustic waves directed at the high-frequency end. The large triple-transit ripples (curve $A$) in the $YZ$ lithium niobate filter are undesirable in many applications. Use of a low-coupling $YX$ quartz substrate represents a method of sacrificing insertion loss for increased triple-transit suppression, because the low $k^2$ reduces the impedance discontinuity parameter to $\tau = 1.0011$. Curve $D$ of Fig. 10 shows the insertion loss function of a $YX$ quartz filter. The insertion loss is increased to 42 dB, but the triple-transit ripples are discernible only on the expanded scale. The computed triple-transit suppression (including the impedance discontinuities) is $2L_{11} = 43$ dB.

## V. EXPERIMENTAL RESULTS

Several experiments have been performed in order to test the circuit model theory including apodization and acoustic impedance discontinuity effects for nonperiodic arrays. The first experiment was designed to test the accuracy of the circuit model prediction for the characteristics of an *unapodized* nonperiodic array.

A 10-$\mu$s delay line was fabricated using two identical transducer arrays deposited in the nondispersive configuration shown in Fig. 11. Each array contained 211 electrodes and, like the example discussed in Section III,
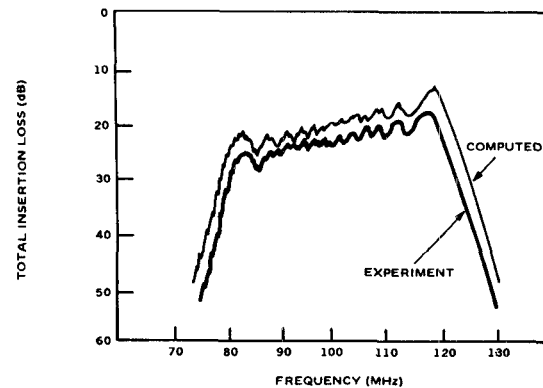


Fig. 12.   Insertion loss of a nondispersive delay line with unapodized linear FM transducers.

was designed according to (35) with $T = 1.05$ $\mu$s, $f_0 = 100$ MHz, and $\Delta = 46.7$ MHz. However, the transducers were unapodized with all $w_n = 0.62$ mm, giving $Q_L = 1$ with 50-$\Omega$ resistive "loads" (generator and receiver). $Y$-cut lithium niobate was employed as the delay medium with surface-wave propagation along the $Z$ axis. The electrode width was fixed at $L_s = 8.7$ $\mu$m along the entire array. The transducer patterns were photoetched from 500-Å thick aluminum and contacted using compression bonded gold leads. Reflectionless acoustic terminations were implemented at the ends of the substrate by rounding the corners in a fashion similar to that employed in a wrap-around surface-wave delay line [20], and roughening the back surface.

The theoretical insertion loss for the delay line was computed for the same electrode spacings, dimensions, and electrical loading conditions as implemented in the measured line, except that no attempt was made to include propagation losses or electrical conduction losses in the theoretical curve. The experimental and theoretical insertion loss data are plotted in Fig. 12. The agreement between the measured and calculated curves is seen to be very good except for an overall difference of approximately 3 dB. This difference in insertion loss across the passband is attributed primarily to propagation attenuation plus a small contribution from the electrical resistance of the arrays. Diffraction loss should not contribute significantly since the output transducer is well within the near-field region of the input transducer on $YZ$ lithium niobate.
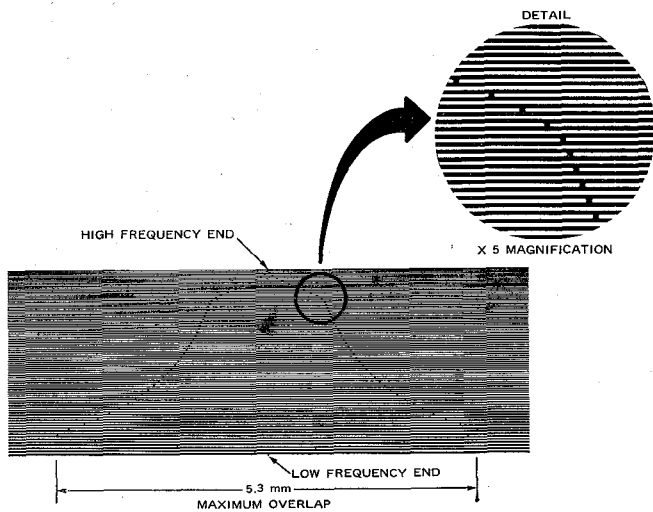
Fig. 13.   Photograph of an apodized broad-band
linear FM transducer.



Fig. 14.   Comparison of computed and measured insertion loss for
an octave-bandwidth nondispersive delay line.

The measured triple-transit echo was 29 dB below the main delayed signal at the midband frequency of 100 MHz. The value of triple-transit echo suppression which was computed neglecting the electrode impedance discontinuity (but including 6 dB for the added propagation loss of the multiple echo) was 51 dB, in serious disagreement with the experiment. When recomputed, however, using an impedance discontinuity parameter of $\tau = 1.022$, the resulting echo suppression was 28 dB, in excellent agreement with the measured value. The high echo suppression measured in this delay line is consistent with a low level of "triple-transit ripple" on the insertion loss function. Since this ripple is less than 0.6 dB (peak to peak) it is not shown in Fig. 12.

In order to test the circuit model predictions for an *apodized* nonperiodic array, a nondispersive delay line was fabricated in a similar configuration to that shown in Fig. 11, but utilizing the heavily weighted 97 electrode transducer pattern shown in Fig. 13. This line was designed with a transducer apodization function which suppresses Fresnel ripple and eliminates the insertion loss taper that is characteristic of an unweighted transducer (see Fig. 12). The apodization is again obtained from (27) using a tapered envelope similar to that specified in (40).

The electrodes were designed so that the electrode width equaled the adjacent gap width $(L_{gn} = L_{sn})$ throughout these arrays. As shown in Fig. 13, passive electrodes were included to obtain straight-crested wavefronts [6]. The input and output transducers were spaced to give an 11.0-$\mu$s delay. Fabrication of the arrays on $YZ$ lithium niobate was quite similar to that described above for the 40-percent bandwidth delay line.

The measured insertion loss for the apodized delay line is compared with the circuit model calculations (including an electrode impedance discontinuity parameter $\tau = 1.022$) in Fig. 14. Once again, no propagation, diffraction, or conduction losses are included in the computed
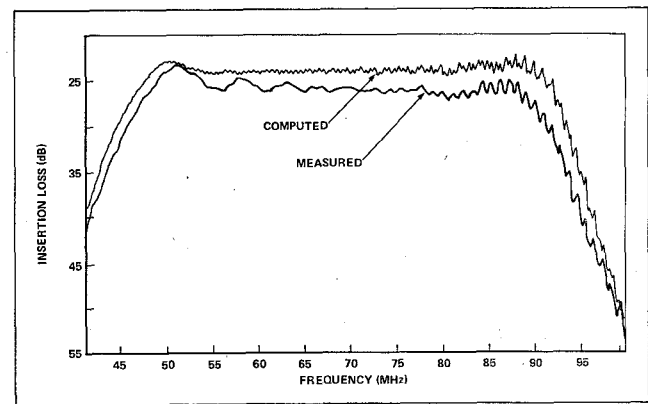
curve. The agreement between theory and experiment is in general quite good. Two points of comparison do require further discussion. First, there is a noticeable insertion loss taper in the measured data across the passband, which is not present in the computed curve. Since the transducer operates over nearly a full octave, it is reasonable to expect the acoustic propagation loss to increase by at least a factor of two across the passband. The difference in level and slope between the theory and measurement can be described by the empirical loss term

$$\text{PL} \cong 0.18 \left( \frac{f}{f_0} \right) \quad (\text{dB}/\mu\text{s}) \tag{42}$$

where $f_0 = 70$ MHz. This loss is considered to be reasonable for lithium niobate at low frequencies. Acoustic losses in the electrodes and the possible excitation of volume waves may also contribute to the total loss although multiple-transit surface-wave echoes were the only spurious delayed pulses observed. The second point relates to the level of "Fresnel" ripple at the low-frequency edge of the passband. The measured ripple amplitude in this region is approximately twice that computed. This suggests that the efficiency of the "cosine squared" tapered electrodes at the low-frequency end of the transducer does not decrease as a smooth function. This behavior may signify that the apodization approximation is breaking down in the low-frequency region because the relative overlap of adjacent electrodes changes quite rapidly (cf., Fig. 13). On the other hand, the analysis and associated apodization technique appear to be valid over the remainder of the delay-line passband where the electrode overlap changes more slowly.

A sensitive test of the impedance discontinuity and apodization aspects of the circuit model lies in the prediction of the triple-transit echo level of the apodized broad-band delay line. A comparison of the measured and predicted echo level is shown in Fig. 15. When the computed echo level is corrected to include three times the propagation loss observed in Fig. 14, the agreement
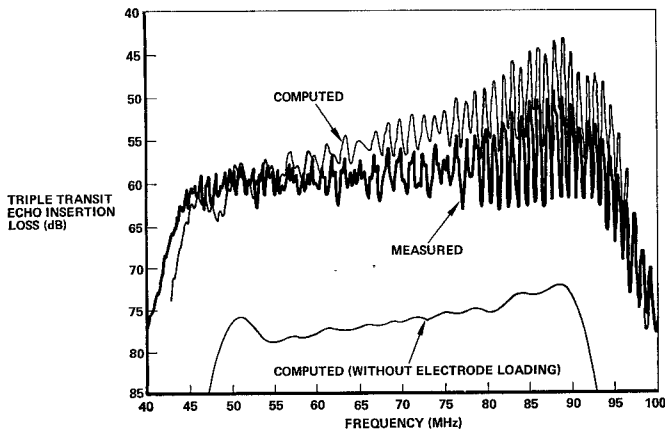
Fig. 15. Comparison of computed and measured triple-transit echo insertion loss for an octave-bandwidth nondispersive delay line.

between theory and experiment is excellent. It is also quite clear that the echo level does not agree with the value predicted when the electrode impedance discontinuity is neglected in the computation.

In addition to confirming predictions of the circuit model, the apodized broad-band delay-line performance demonstrates the value of Section III for the design of filters having specified bandshape characteristics.

## APPENDIX A

### ADMITTANCE MATRIX OF A DISPERSIVE TRANSDUCER

Fig. 3 illustrates the crossed-field Mason circuit for one electrode, neglecting the fact that the metallized and unmetallized regions have slightly different acoustic propagation characteristics. Defining the usual admittance matrix $y_{ij}$ for this electrode $i_i = \sum_{j=1}^{3} y_{ij}e_j$, we find from circuit analysis $y_{ij} = y_{ji}$ and, letting $Z_0 = 1$,

$$y_{11} = y_{22} = -j \cot \theta$$

$$y_{12} = j \csc \theta$$

$$y_{13} = y_{23} = -jr \tan \frac{\theta}{2}$$

$$y_{33} = j\left( \omega C + 2r^2 \tan \frac{\theta}{2} \right). \qquad \text{(A-1)}$$

In order to include the effects of surface metallization on acoustic propagation, it is necessary to use the modified circuit of Fig. 8. This circuit subdivides the unit cell into metallized and unmetallized regions having different acoustic impedances and velocities. We can let $Z_0 = 1$ and $Z_m = 1/\tau$ without loss of generality; we now find from circuit analysis the more complicated admittance coefficients

$$y_{11} = y_{22} = jd[c + e \cot \phi]$$

$$y_{12} = jd\tau \csc^2 \phi \csc \psi$$

$$y_{13} = y_{23} = -jr \tan \frac{\phi}{2} - jabd \csc \phi$$

$$y_{33} = j\left\{ 2\pi fC + 2r\left( a + r \tan \frac{\phi}{2} \right) \right. $$
$$\left. + \frac{a^2}{c} (1 + b^2 d) \right\} \qquad \text{(A-2)}$$

where $a$, $b$, $c$, $d$, and $e$ are auxiliary functions of $\psi$ and $\phi$, given by

$$a = r\left( \tau \tan \frac{\psi}{2} + \tan \frac{\phi}{2} \right)$$

$$b = \cot \phi + \tau \cot \frac{\psi}{2}$$

$$c = \tau \cot \psi + \cot \phi$$

$$d = (c \cot \phi - e)^{-1}$$

and

$$e = \tau(\tau - \cot \phi \cot \psi). \qquad \text{(A-3)}$$

The structure of an entire transducer array is represented by interconnecting the Mason circuits as shown in the block diagram of Fig. 5. We cascade terminals 1 of section $n$ into terminals 2 of section $(n+1)$ and connect all sets of terminals 3 in parallel. The alternating electric polarities of successive sections are accounted for by $r_n$. We define "cumulative" $\tilde{y}_{ij}^{(n)}$ coefficients by

$$\tilde{y}_{ij}^{(1)} = y_{ij}^{(1)} \qquad \text{(A-4)}$$

and, for $n > 1$, the recursion relations

$$\tilde{y}_{11}^{(n)} = y_{11}^{(n)} - \frac{[y_{12}^{(n)}]^2}{D}$$

$$\tilde{y}_{12}^{(n)} = \frac{-y_{12}^{(n)}\tilde{y}_{12}^{(n-1)}}{D}$$

$$\tilde{y}_{22}^{(n)} = \tilde{y}_{22}^{(n-1)} - \frac{[\tilde{y}_{12}^{(n-1)}]^2}{D}$$

$$\tilde{y}_{13}^{(n)} = y_{13}^{(n)} - \frac{y_{12}^{(n)}y'}{D}$$

$$\tilde{y}_{23}^{(n)} = \tilde{y}_{23}^{(n-1)} - \frac{\tilde{y}_{12}^{(n-1)}y'}{D}$$

$$\tilde{y}_{33}^{(n)} = y_{33}^{(n)} + \tilde{y}_{33}^{(n-1)} - \frac{(y')^2}{D}$$

$$\tilde{y}_{ij} = \tilde{y}_{ji} \qquad \text{(A-5)}$$

where

$$D = y_{22}^{(n)} + \tilde{y}_{11}^{(n-1)} \qquad \text{(A-6)}$$

and

$$y' = y_{23}^{(n)} + \tilde{y}_{13}^{(n-1)}. \qquad \text{(A-7)}$$

The $Y_{ij}$ coefficients of an $N$-section transducer are of course just equal to $\tilde{y}_{ij}^{(N)}$.

# APPENDIX B

## TRANSFER FUNCTION OF A TRANSDUCER

This appendix derives the transfer function of a transducer described by the circuit model discussed in Section II. The desired transfer function is

$$T_{13}(f) = \frac{2}{\sqrt{Z_0 G_L}} \frac{E_1}{E_g} \tag{B-1}$$

which obtains when the transducer is connected as in Fig. 6(a). We first calculate the ratio $E_1/E_3$, which corresponds to finding $E_1$ when an ideal voltage generator ($G_L = \infty$) is connected to port 3. By inspecting the transducer circuit (Fig. 5) and letting each of the $N$ unit cells have the form shown in Fig. 3, we see that a short circuit on the electric port causes the acoustic transmission lines to pass acoustic waves without reflection. With the Mason transformers shorted, the acoustic transmission lines are completely decoupled from the electric circuit. Thus the $N$ electrodes behave as a set of noninteracting acoustic sources or receivers, and for the launch transducer case we can find the acoustic force ($E_1$) by summing (with appropriate phasors) the acoustic stress amplitudes generated at the $N$ electrodes.

In order to find the stress amplitude generated by *one electrode*, we use the $y_{ij}$ coefficients given by (A-1) and place matched acoustic loads ($Z_0 = 1$) on the acoustic ports of the one-electrode Mason circuit (Fig. 3). We thus find that the $n$th electrode launches acoustic stress waves in both directions, whose acoustic force (referred to the electrode center) is

$$F_n = jE_3 r_n \sin\left(\frac{\pi}{2} \frac{f}{f_n}\right). \tag{B-2}$$

Multiplying $F_n$ by the phasor $\exp(-j2\pi f t_n)$ corresponds to propagation to the end of the transducer (i.e., to port 1 or 2) where all the waves are summed to yield the total acoustic force $E_1$, namely,

$$E_1 = jE_3 \sum_{n=1}^{N} r_n \sin\left(\frac{\pi}{2} \frac{f}{f_n}\right) \exp(-j2\pi f t_n). \tag{B-3}$$

In order to find the desired transfer function $T_{13}(f)$ we must recognize that $E_3 \neq E_g$ when a real generator (finite $G_L$) is used. However, we note that

$$E_3 = E_g \frac{G_L}{G_L + Y_{in}(f)} \tag{B-4}$$

where $Y_{in}(f)$ is the transducer input admittance, given by

$$Y_{in}(f) = j\omega C_T + Y_{rad}(f). \tag{B-5}$$

$Y_{rad}(f)$ is the radiation admittance, defined in terms of

$Y_{ij}$ by

$$Y_{rad}(f) = (Y_{33} - j\omega C_T) - \tfrac{1}{2}(Y_{13}{}^2 + Y_{23}{}^2)$$
$$+ \frac{Y_{12} Y_{13} Y_{23}}{1 + Y_{11}}. \tag{B-6}$$

Equations (B-1) through (B-6) can be combined directly to give an expression for $T_{13}(f)$, but the most useful form results if we also employ the quantities $Q_r$, $Q_L$, $r_n'$, and $y_{rad}$ defined in Section III. Straightforward substitution gives the desired result

$$T_{13}(f) = \sqrt{\frac{2Q_L}{Q_r}} \frac{\displaystyle\sum_{n=1}^{N} r_n' \sin\left(\frac{\pi}{2} \frac{f}{f_n}\right) \exp(-j2\pi f t_n)}{1 + jQ_L \dfrac{f}{f_0} + \dfrac{Q_L}{Q_r} y_{rad}(f)} \cdot \tag{B-7}$$

Because of the way the acoustic forces (B-2) add to give $E_1$ (B-3), it follows that $|E_2| = |E_1|$, and thus $|T_{13}| = |T_{23}|$.

# APPENDIX C

## SPECTRUM OF A SAMPLED TIME WAVEFORM

Consider the time signal

$$g(t) = a(t) \exp[j\theta(t)] \tag{C-1}$$

sampled as in the left-hand side of (22) in Section III. The Fourier transform (spectrum) of the sampled version of this signal is given by

$$G(f) = \int_{-\infty}^{\infty} \sum_{n=1}^{N} a(t) \exp[j\theta(t)] \{\delta[\theta(t) - (n + \tfrac{1}{2})\pi]$$
$$+ \delta[\theta(t) - (n - \tfrac{1}{2})\pi]\} \exp(-j2\pi f t)\, dt$$
$$= \sum_{n=1}^{N} \left\{ \frac{a(t_{n+1/2}) \exp[j(n + \tfrac{1}{2})\pi - j2\pi f t_{n+1/2}]}{\dot{\theta}(t_{n+1/2})} \right.$$
$$\left. + \frac{a(t_{n-1/2}) \exp[j(n - \tfrac{1}{2})\pi - j2\pi f t_{n-1/2}]}{\dot{\theta}(t_{n-1/2})} \right\} \tag{C-2}$$

where

$$\theta(t_{n\pm1/2}) = (n \pm \tfrac{1}{2})\pi. \tag{C-3}$$

$G(f)$ may be simplified by assuming that $g(t)$, $a(t)$, and $\theta(t)$ are slowly varying. Pursuant to this assumption we expand $\theta(t)$ and $t_n$ and obtain

$$t_{n\pm1/2} \cong t_n \pm \frac{1}{4f_n} \tag{C-4}$$

where

$$f_n = \frac{\dot{\theta}(t_n)}{2\pi} \cong \frac{\dot{\theta}(t_{n+1/2})}{2\pi} \tag{C-5}$$

is the instantaneous frequency.

These approximations, together with $a(t_{n\pm1/2}) \cong a(t_n)$, enable us to write

$$G(f) \cong \frac{1}{\pi} \sum_{n=1}^{N} \frac{(-1)^n a(t_n)}{f_n} \sin\left(\frac{\pi}{2} \frac{f}{f_n}\right) \exp\left(-j2\pi f t_n\right). \quad (C-6)$$

The factor $\sin\left((\pi/2)(f/f_n)\right)$ is a direct consequence of sampling according to (C-2), which corresponds to the correct representation of the crossed-field circuit model by delta-function samples.

## ACKNOWLEDGMENT

## REFERENCES

[1] R. H. Tancrell and M. G. Holland, "Acoustic surface wave filters," *Proc. IEEE*, vol. 59, pp. 393–409, Mar. 1971.
[2] W. D. Squire, H. J. Whitehouse, and J. M. Alsup, "Linear signal processing and ultrasonic transversal filters," *IEEE Trans. Microwave Theory Tech.*, vol. MTT-17, pp. 1020–1040, Nov. 1969.
[3] R. H. Tancrell, M. B. Shulz, H. H. Barrett, L. Davis, Jr., and M. G. Holland, "Dispersive delay lines using ultrasonic surface waves," *Proc. IEEE* (Lett.), vol. 57, pp. 1211–1213, June 1969.
[4] P. Hartman and E. Dieulesant, "Acoustic surface wave filters," *Electron. Lett.*, vol. 5, pp. 657–658, 1969.
[5] ——, "Intrinsic compensation of sidelobes in a dispersive acoustic delay line," *Electron. Lett.*, vol. 5, pp. 219–220, May 1969.
[6] H. M. Gerard, G. W. Judd, and M. E. Pedinoff, "Phase corrections for weighted acoustic surface-wave dispersive filters," *IEEE Trans. Microwave Theory Tech.* (Corresp.), vol. MTT-20, pp. 188–192, Feb. 1972.
[7] W. R. Smith, H. M. Gerard, J. H. Collins, T. M. Reeder, and H. J. Shaw, "Analysis of interdigital surface wave transducers by use of an equivalent circuit model," *IEEE Trans. Microwave Theory Tech.*, vol. MTT-17, pp. 856–864, Nov. 1969.
[8] G. A. Coquin and H. F. Tiersten, "Analysis of the excitation and detection of piezoelectric surface waves in quartz by means of surface electrodes," *J. Acoust. Soc. Amer.*, vol. 41, pp. 921–939, Apr. 1967.
[9] J. J. Campbell and W. R. Jones, "A method for estimating optimal crystal cuts and propagation directions for excitation of piezoelectric surface waves," *IEEE Trans. Sonics Ultrason.*, vol. SU-15, pp. 209–217, Oct. 1968.
[10] W. R. Smith and H. M. Gerard, "Differences between in-line and crossed-field three-port circuit models for interdigital transducers," *IEEE Trans. Microwave Theory Tech.* (Corresp.), vol. MTT-19, pp. 416–417, Apr. 1971.
[11] H. M. Gerard and W. R. Smith, "Design of broadband surface wave transducers using an equivalent circuit model," in *1970 IEEE Ultrason. Symp. Dig.*, p. 27.
[12] H. Skeie, "Electrical and mechanical loading of a piezoelectric surface supporting surface waves," *J. Acoust. Soc. Amer.*, vol. 48, pt. II, pp. 1098–1109, Nov. 1970.
[13] B. A. Auld, "Surface wave theory," in *Invited Proc. 1970 IEEE Ultrason. Symp.*, Oct. 1971.
[14] C. C. Tseng, "Elastic surface waves on free surface and metallized surface of CdS, ZnO and PZT-4," *J. Appl. Phys.*, vol. 38, pp. 4281–4284, Oct. 1967.
[15] H. F. Tiersten, "Elastic surface waves guided by thin films," *J. Appl. Phys.*, vol. 40, pp. 770–789, Feb. 1969.
[16] C. Lardat, C. Maerfeld, and P. Tournois, "Theory and performance of acoustical dispersive surface wave delay lines," *Proc. IEEE*, vol. 59, pp. 355–368, Mar. 1971.
[17] S. G. Joshi and R. M. White, "Dispersion of surface elastic waves produced by a conducting grating on a piezoelectric crystal," *J. Appl. Phys.*, vol. 39, pp. 5819–5827, Dec. 1968.
[18] E. K. Sittig and G. A. Coquin, "Filters and dispersive delay lines using repetitively mismatched ultrasonic transmission lines," *IEEE Trans. Sonics Ultrason.*, vol. SU-15, pp. 111–119, Apr. 1968.
[19] W. S. Jones, C. S. Hartman, and T. D. Sturdivant, "Modified equivalent circuit model for ultrasonic surface wave interdigital transducers," in *1971 IEEE-G-MTT Symp. Dig.*, pp. 58–59.
[20] W. L. Bond, T. M. Reeder, and H. J. Shaw, "Wrap-around surface wave delay lines," *Electron. Lett.*, vol. 7, pp. 79–80, Feb. 1971.